HHS Public Access

Author manuscript

Wound Repair Regen. Author manuscript; available in PMC 2022 April 12.

Published in final edited form as:

Wound Repair Regen. 2022 January ; 30(1): 82–99. doi:10.1111/wrr.12984.

The lysosomal trafficking regulator is necessary for normal wound healing

Jacob C. Zbinden, MS[1,2], **Gabriel J. M. Mirhaidari, PhD**[1,3], **Kevin M. Blum, PhD**[1,2], **Andrew J. Musgrave, BS**[1], **James W. Reinhardt, PhD**[1], **Christopher K. Breuer, MD**[1], **Jenny C. Barker, MD, PhD**[1,4]

[1]Center for Regenerative Medicine, Abigail Wexner Research Institute at Nationwide Children's Hospital, Columbus, Ohio, USA

[2]Department of Biomedical Engineering, The Ohio State University, Columbus, Ohio, USA

[3]Biomedical Sciences Graduate Program, The Ohio State University College of Medicine, Columbus, Ohio, USA

[4]Department of Plastic and Reconstructive Surgery, The Ohio State University Wexner Medical Center, Columbus, Ohio, USA

Abstract

Non-healing wounds are a major threat to public health throughout the United States. Tissue healing is complex multifactorial process that requires synchronicity of several cell types. Endolysosomal trafficking, which contributes to various cell functions from protein degradation to plasma membrane repair, is an understudied process in the context of wound healing. The lysosomal trafficking regulator protein (LYST) is an essential protein of the endolysosomal system through an indeterminate mechanism. In this study, we examine the impact of impaired LYST function both in vitro with primary LYST mutant fibroblasts as well as in vivo with an excisional wound model. The wound model shows that LYST mutant mice have impaired wound healing in the form of delayed epithelialization and collagen deposition, independent of macrophage infiltration and polarisation. We show that LYST mutation confers a deficit in MCP-1, IGF-1, and IGFBP-2 secretion in beige fibroblasts, which are critical factors in normal wound healing. Identifying the mechanism of LYST function is important for understanding normal wound biology, which may facilitate the development of strategies to address problem wound healing.

Correspondence: Jenny C. Barker, Department of Plastic and Reconstructive Surgery, The Ohio State University Wexner Medical Center, Columbus, OH 43210, USA. jenny.barker@osumc.edu.
Jacob C. Zbinden and Gabriel J. M. Mirhaidari contributed equally to this work.

CONFLICT OF INTEREST

Christopher K. Breuer is a founder of LYST Therapeutics, LLC (OH, USA) and a portion of this work was supported by a sponsored research agreement from LYST Therapeutics, LLC. The authors have no other relevant affiliations or financial involvement with any organisation or entity with a financial interest in or financial conflict with the subject matter or materials discussed in the manuscript apart from those disclosed.

SUPPORTING INFORMATION

Additional supporting information may be found in the online version of the article at the publisher's website.

Keywords

epithelialization; IGF-1; IGFBP-2; lysosomal trafficking regulator; LYST; MCP-1; wound healing

1 | INTRODUCTION

In 2019, 8.2 million Medicare beneficiaries in the United States were wound care patients with a cost of care ranging from $28.1 to $96.8 billion,[1] highlighting the enormous public health burden of non-healing wounds. To address this growing problem, an expanded understanding of fundamental processes of normal wound healing is necessary to provide new targets for therapeutic consideration. Despite the biologic importance and phylogenetic conservation, basic understanding of wound biology is limited for certain fundamental and critical cell processes including endolysosomal-mediated protein trafficking. We sought to investigate the role of a protein at the centre of the endolysosomal system, the lysosomal trafficking regulator (LYST), in the context of cutaneous wound healing.

LYST encodes a protein of approximately 430 kDa that is involved with vesicle size and trafficking through an unknown mechanism. Homozygous germline mutations in LYST cause Chediak-Higashi syndrome (CHS), a rare autosomal recessive disease, and the beige (Bg) mouse analogue.[2–5] For the Bg mouse, specifically, a three base-pair deletion resulting in a single isoleucine loss near the C-terminus is sufficient to disrupt protein function. CHS and Bg mutations result in phenotypic enlarged cellular granules including lysosomes, melanosomes, platelet dense bodies, and other lysosome related organelles.[6–9] Debate still exists as to whether the enlarged granules are a result of abnormal fusion,[10–12] decreased fission,[5,13] or a combination.[14] Prior work has predominately characterised the role of LYST in cytotoxic lymphocytes and platelets due to the susceptibility of CHS patients to infection.[9,15–18] However, LYST is ubiquitously expressed in other tissues and cell types including fibroblasts.[19] The exact molecular mechanisms by which LYST functions are still unknown, especially in areas outside of inflammation and thrombosis.

We characterised the wound healing impact of the LYST mutation, in vivo, using a splinted excisional murine model of wound healing in Bg mice. Findings revealed that the LYST mutation confers delayed wound healing of skin, hallmarked by decreased collagen and delayed epithelialization, independent of macrophage infiltration and polarisation. Due to fibroblast importance in inflammation/tissue repair, we sought to characterise tissue-healing mediators derived from LYST mutant fibroblasts, in vitro. We hypothesised that LYST mutant fibroblasts would have abnormal protein secretion (e.g., growth factors, cytokines, chemokines) compared to control fibroblasts due to dysregulation of lysosomal trafficking. We found that MCP-1, IGF-1, and IGFBP-2 were all present in lower levels in media derived from primary LYST mutant fibroblasts harvested from Bg mice compared to wild type mice controls. Together, these findings highlight the importance of endolysosomal trafficking in normal cutaneous wound healing, and define a role for LYST, specifically, in this process.

2 | MATERIALS AND METHODS

2.1 | Animals

The Nationwide Children's Hospital Institutional Animal Care and Use Committee approved all experimental procedures involving animals. All animals received care in compliance with the National Institutes of Health (NIH) Guide for the Care and Use of Laboratory Animals (NIH, Bethesda, MD, USA). Wild type (WT) (C57BL/6J) and beige (Bg) (C57BL/6J-Lyst$^{bg\text{-}J}$/J) mice were purchased from The Jackson Laboratory (Bar Harbor, ME, USA). Male mice 8–12 weeks of age were used for wound healing experiments.

2.2 | Splinted excisional wound model

For wound healing assessment, 30 WT and 30 Bg mice were divided into cohorts of 10 mice that were sacrificed at specific time points (3, 7, and 28 days). A splinted excisional model was used as previously described.[20,21] Briefly, mice were anaesthetised and shaved to expose the dorsal surface. Sterile scissors were used to create full-thickness wounds approximately 6 mm in diameter extending through the panniculus carnosus muscle. A silicone ring, 13 mm internal diameter and 0.8 mm thick (Grace Bio-Labs, OR, USA), was secured with 3–0 nylon suture around the wound to prevent the panniculus carnosus from contracting. Mastisol® (Eloquest Healthcare®, Inc., MI, USA) liquid adhesive was applied around the outer edge of the splint to improve adherence of the surgical dressing that consisted of Tegaderm™ (3M™, MN, USA) followed by an elastic bandage wrap (Gentle Tape, CVS Health™, RI, USA). Mice were housed in individual cages and allowed to fully recover in an incubator at 32°C until they became mobile.

2.3 | Wound evaluation

Mice were monitored daily to ensure the dressings and splints remained in place. Wounds were evaluated at 0, 3, 7, 10, and 14 days for 2-D planimetry analysis and then followed until complete healing. Wounds were imaged with a Leica M80 microscope (Leica Camera AG, Germany). Image files were blinded, and wound area measurements were made using ImageJ (NIH, MD, USA). Wound area values were normalised to the initial wound area. Different cohorts of mice were sacrificed at days 3, 7, and 28 post excision.

2.4 | Mechanical testing

To assess the strength of healed skin, biopsies (30 mm × 80 mm) were obtained from the healed scar 28 days after wounding. Non-wounded control samples were simultaneously harvested from each animal. Each rectangular-shaped skin biopsy was stored in a 50 ml polypropylene conical tube containing normal saline solution and placed in ice for 2–4 h until cut into a dog bone–shaped specimen (gauge length of 5 mm and gauge width of 3 mm) for tensile testing. The harvested skin was placed in a position such that the biopsied site was in the centre of the gauge length and width. Each specimen was then mounted into the grips of a TestResources mechanical tester model 1000R12 (TestResources, MN, USA) with a 2.2 lbf load cell. All skin samples were strained at a rate of 2 mm/s until failure and maximum load was recorded in newtons (N).

2.5 | Transepidermal water loss

A separate cohort of WT and Bg male mice (n = 10 per group) were shaved, and the epithelial barrier was disrupted with repeated abrasion using surgical tape as previously described.[22] 10–15 tape applications per mouse resulted in a repeatable and measurable disruption of barrier function, but without creation of a wound. Transepidermal water loss (TEWL) was measured as an assessment of barrier function of the skin prior to the procedure and at 0, 1, 3, 6, and 24 h post procedure. TEWL was obtained by measuring the humidity of the air directly above the skin relative to the humidity in the ambient environment using a DermaLab® Combo (Cortex Technology ApS, Denmark). TEWL was calculated as grams of water lost per square metre of skin per hour. Higher values indicate more water loss and therefore less barrier function. TEWL measurements were taken three times at each time point on each animal and averaged to account for variability. TEWL measurements of wounds were normalised to the pre- and post-procedure TEWL readings to determine the % recovery through the following formula:

$$\%\text{Recovery} = \frac{\text{Post}-\text{Current}}{\text{Post}-\text{Pre}} \times 100\%$$

where *Pre*, *Post*, and *Current* represent the average TEWL recordings immediately before adhesive stripping, after adhesive stripping, and at the current time point, respectively.

2.6 | Histology and immunohistochemistry

Wounds from day 3 and day 7 cohorts were excised from mice following euthanasia. Scar and surrounding skin were fixed with pins to keep tissue in a flattened shape then fixed in 10% formalin for 24 h at 4°C. Fixed samples were paraffin-embedded and 4 μm thick sections were mounted onto slides. Tissue sections were stained with H&E, Picro-Sirius Red, and Movat's Pentachrome using standard techniques to examine cellularity, collagen, and other extracellular matrix constituents. For immunohistochemistry, slides were first deparaffinised in xylene followed by serially diluted alcohol washes. Antigen retrieval was performed utilising a citrate buffer with pH 6.1 (Cat# S1699, Agilent Technologies, CA, USA). Sections were blocked for endogenous peroxidase activity with 3% hydrogen peroxide (Thermo Fisher Scientific, MA, USA) followed by blocking for background with 3% normal goat serum (NGS) (Cat# S-1000–20, Vector Laboratories, CA, USA) in Background Sniper (Cat# BS966M, Biocare Medical, LLC, CA, USA) for 1 h at room temperature. Sections were incubated with primary antibody diluted in Antibody Diluent, Background Reducing (Cat# S3022, Agilent) overnight at 4°C. Primary antibodies and dilutions used were as follows; Cytokeratin (1:500, Cat# 9377, Abcam PLC, UK), Ki67 (1:2000, Cat# 15580, Abcam), F4/80 (1:500, Cat# 16911, Abcam), CD68 (1:2000, Cat# 125212, Abcam), iNOS (1:250, Cat# 15323, Abcam), CD206 (1:8000, Cat# 64693, Abcam), CD31 (1:500, Cat# 28364, Abcam), MMP-1 (1:1000, Cat# bs-0463R, Sapphire Bioscience, Redfern, Australia), TIMP-1 (1:2000, Cat# 211926, Abcam) and MMP-9 (1:1000, Cat# 38898, Abcam). Slides were then stained with appropriate secondary biotinylated antibodies (Vector Laboratories) at a 1:1500 dilution in PBS for 1 h at room temperature. Slides were subsequently incubated in streptavidin horseradish peroxidase (Cat# PK-7100, Vector Laboratories) with colour development with 3,3-diaminobenzidine (Cat# SK-4105, Vector

Laboratories), and nuclei counterstaining with Gill's haematoxylin (Cat# H-3401–500, Vector Laboratories). Slides underwent dehydration in alcohol and clearing xylene before applying cover slips with mounting medium (Cat# H-5000–60, Vector Laboratories).

2.7 | Primary fibroblast culture

Cultures were prepared as previously described.[21] Briefly, primary fibroblasts were isolated from ear biopsies of 2-to 6-month-old Bg and WT mice (2–3 mice per fibroblast line). For each experiment conducted (antibody array, ELISA, immunofluorescence staining, RT-qPCR) new fibroblast lines were derived. Ear samples were minced and digested for 1 h in collagenase/dispase (4 mg/ml) in one well of a 24-well plate. One millilitre of fibroblast media (Dulbecco's Modified Eagle Medium, 16% foetal bovine serum, penicillin/streptomycin, L-glutamine, amphotericin B) was then added and cells were incubated overnight at 37°C in low oxygen conditions (5%). Cells were then triturated, filtered with a 70 μm cell strainer and cultured in fibroblast media and allowed to recover. All cells used for experimental purposes were subsequently passaged once into serum-free media containing basic fibroblast growth factor (Catalogue# M2267SF-Kit, Cell Biologics, IL, USA) and 200 μM ascorbic acid.

For the migration assay, fibroblasts were derived as stated above and followed previously published protocols.[23] Briefly, cells were plated in 6-well tissue culture treated dishes with inserts (Ibidi Cat# 80209) added at time of plating to create a divided space for cells to migrate across. Images were captured at the indicated time points after insert removal on a ZEISS AxioImager.A2 microscope with a Zeiss AxioCam MRc 5 (colour) digital camera.

2.8 | Mouse protein antibody array and ELISAs

Conditioned media from passage one primary fibroblasts was harvested 24 h after the first passage and applied to a 96 protein RayBiotech Mouse Cytokine Antibody Array (Cat# AAM-CYT-1000, RayBiotech, GA, USA) and processed according to the manufacturer's protocol. Chemiluminescence with film development was used for positive spot detection and semi-quantitative analysis of signal intensity was performed using ImageJ.[24,25] Background intensity was subtracted out and measurements were normalised relative to positive controls on each membrane.

Mouse monocyte chemoattractant protein-1 (MCP-1; Cat# ELM-MCP-1), insulin-like growth factor-1 (IGF-1; Cat# ELM-IGF1–1), and insulin-like growth factor binding protein-2 (IGFBP-2; Cat# ELM-IGFBP2–1) quantitative ELISAs from RayBiotech were used for detection and quantification of protein secretion. Experiments were performed according to the manufacturer's guidelines and quantified for absorbance values read on a SpectraMax M5 (Molecular Devices, CA, USA).

2.9 | RT-qPCR analysis

Cultured fibroblasts were removed from plates with 0.25% trypsin, centrifuged, and washed in PBS at 24-, 48-, and 72-h intervals after the first passage. Cells were stored in RNA*later* Stabilisation Solution (Cat# AM7020, Thermo Fisher Scientific) at –80°C until RNA extraction. RNA extraction was performed with the Zymo *Quick*-RNA Miniprep

kit (Cat# R1054, Zymo Research, CA, USA) according to the manufacturer's protocol. Genomic DNA was removed using a DNA eliminator spin column followed with on column DNA digestion with DNAse I. RNA was then processed with the Zymo RNA Clean & Concentrator Kit (Cat# R1031).

For gene expression analysis of wound samples, surgery was performed as described above. At time of surgery, excised skin was snap frozen in liquid nitrogen to serve as a baseline control (non-wounded skin) for comparison to excised wounded skin at days 3, 7, and 10. At time of sacrifice, wounded skin was excised and snap frozen in liquid nitrogen. For RNA extraction, RNase clean mortar and pestles were pre-chilled in liquid nitrogen. Normal skin and wounded skin samples were ground into a fine powder in the pre-chilled pestles. Samples were then processed with the Qiagen RNeasy Fibrous Tissue Mini Kit according to manufacturer instructions (Cat# 74704). Genomic DNA was eliminated via on-column digestion using DNase.

RNA from fibroblasts and skin samples was quantified on a Nandrop2000c for concentration with a 260/280 ratio greater than 2.0. Select samples were analysed on an Agilent Bioanalyzer to validate the protocol with an RNA integrity number greater than 7.0. RNA to cDNA conversion was completed with the Applied Biosystems High-Capacity RNA-to-cDNA kit (Cat# 4387406, Thermo Fisher Scientific) and run on a Verti Fast Thermocycler. Taqman Fast Advanced Master Mix (Cat# 4444557, Thermo Fisher Scientific) with the following hybridization probes were utilised for qPCR of cDNA samples: LYST (Cat# Mm00465000_m1), CCL2 (Cat# Mm00441242_m1), IGF1 (Cat# Mm00439560_m1), IGFBP2 (Cat# Mm00492632_m1), Col1a1 (Cat# Mm00801666_g1), Col1a2 (Cat# Mm00483888_m1), and Col3a1 (Mm00802331_m1). Samples were run on an Applied Biosystems StepOnePlus Real-Time Fast PCR System. Plate design followed a sample maximisation approach with no template controls and reverse-transcriptase negative controls.[26] A pilot run was utilised to determine the most stably expressed reference gene between samples comparing GAPDH (Cat# Mm99999915_g1), ACTB (Cat# Mm02619580_g1), B2M (Cat# Mm00437762_m1), and HPRT (Cat# Mm00446968_m1). Resulting cycle-threshold values were analysed with the online tool RefFinder, a combination of BestKeeper, NormFinder, geNorm, and the comparative delta-Ct method.[27–31] ACTB was determined to be the most stably expressed reference gene for fibroblasts. B2M was determined to be the most stably expressed reference gene for skin samples. Respective reference genes were subsequently used for delta–delta Ct calculations.

2.10 | Immunofluorescence

For cell culture experiments, cells were grown on sterile, gelatin-coated glass cover slips and were fixed at 24 h after the first passage with 4% paraformaldehyde for 20 min at room temperature. Cells were permeabilized and background blocked with 0.3% Triton X-100 + 10% NGS in PBS for 45 min at room temperature. Primary antibodies were diluted in 1% NGS + 0.3% Triton X-100 + 1% BSA in PBS and incubated on slides overnight at 4°C. The primary antibodies and dilutions used were as follows: LAMP-1 (1:1000, Cat# 14–1071-82, Invitrogen, CA, USA), MCP-1 (1:500, Cat# MA5–17040, Invitrogen), IGF-1 (1:250, Cat# PAJ-27207, Invitrogen), and IGFBP-2 (1:250, Cat# MAB797, R&D

Systems, NE, USA). Slides were incubated with appropriate secondary antibodies at a 1:300 dilution (AlexaFluors, Thermo Fisher Scientific). Samples stained for actin were incubated with ActinGreen 488 Ready Probe (Cat# R37110, Invitrogen). Slides were mounted with mounting medium containing DAPI nuclear counterstain (Cat# S36938, Thermo Fisher Scientific). Slides with secondary but no primary antibodies were used as negative background controls.

2.11 | Imaging and quantification

Photomicrographs were acquired with a ZEISS AxioImager.A2 microscope with a Zeiss AxioCam MRc 5 (colour) digital camera or a ZEISS AxioObserver.21 inverted microscope with a ZEISS AxioCam 105 (colour) digital camera (Carl Zeiss AG, Germany). For histological stains (H&E and Picro-Sirius Red), a 10× objective was used and several images were tiled and stitched together to capture the entire wound sample. For immunohistochemical stains (F4/80, iNOS, CD206, MMP-1, MMP-9, TIMP-1) a 40× objective was used to capture four images along the length of the wound bed. The exceptions to this are the stains for Cytokeratin, Ki67, and CD31 that were taken as tiled images of the entire wound bed using a 10× objective. Representative immunofluorescence (IF) images were captured in using a 63× objective and a ZEISS Apotome.2 was used to achieve high focal plane contrast.

Quantification of images was performed using ImageJ (NIH). Cellular and vessel counts were made using pixel specific thresholding based on values of hue, saturation, and brightness as well as size exclusion. These values were chosen based on positive control sections of murine splenic tissue. Values were averaged for stains with multiple images per section. Collagen area of the wounds was measured using similar methods to isolate coloured pixels and normalised to the area of the entire wound bed.

2.12 | Statistical analysis

Data are presented as mean values ± standard deviation. All statistical tests were performed using GraphPad Prism 8.0 (GraphPad Software, CA, USA). A $p \leq 0.05$ was considered statistically significant. Planimetry and TEWL values were compared using two-way repeated measures ANOVA with mouse strain and time being the independent factors and using Geisser–Greenhouse's correction as needed. Sidak's post hoc test was used for multiple comparisons. Relative protein integrated density values, ELISA protein readouts, and healing time were compared with two-tailed Student's *t*-test. Mechanical, histological, and RT-qPCR delta–delta Ct values were compared using two-way ANOVA with independent variables of skin type/mouse genotype for mechanical values and time/mouse genotype for histology and PCR values. Sidak's test was performed post hoc if there was a significant effect of either variable or a significant interaction between variables.

3 | RESULTS

3 1 | Wound closure is delayed in Bg mice

We performed an in vivo assessment of wound healing in wild type (WT) (C57BL/6J) and beige (Bg) (C57BL/6J-Lyst$^{bg\text{-}J}$/J) mice. Full thickness cutaneous wounds (Figure 1A)

were serially monitored, and area measurements (Figure 1B) showed that WT mice had significantly greater wound closure than Bg mice at days 3 ($p = 0.0030$), 10 ($p = 0.0017$), and 14 ($p = 0.0082$). The average number of days to complete healing (Figure 1C) was 3 days longer in Bg mice ($p = 0.0098$). Overall, these data illustrate the delayed healing response in Bg mice.

As expected for a healed wound, normal skin of both WT and Bg mice had greater average max stress (Figure 1D) in comparison to scar tissue 28 days post excision ($p = 0.0378$ for WT, $p = 0.0169$ for Bg). The scar tissue of Bg mice was stiffer (Figure 1E) on average than normal skin of Bg mice ($p = 0.0444$), while there was not a difference between WT normal and scar skin stiffness. No significant differences in max stress or stiffness were seen between WT and Bg mice.

3 2 | Bg mice have normal macrophage presence and vascularization

Anti-F4/80 was used to assess the presence of macrophages in the wound bed (Figure 2A,B). The number of F4/80+ cells per high-powered field (HPF) decreased significantly in WT wound between days 3 and 7 ($p = 0.0149$) while Bg did not ($p = 0.4327$). Similar results were seen with the neutrophil marker MPO (Figure 2C), where WT wounds saw a decrease in MPO+ cells between days 3 and 7 ($p = 0.0404$) while Bg did not ($p = 0.6496$). Antibodies against iNOS (Figure 2D) and CD206 (Figure 2E) were used to identify inflammatory and anti-inflammatory macrophages, respectively. The average number of iNOS+ cells increased significantly between days 3 and 7 in Bg wounds ($p = 0.0022$) but not in WT wounds ($p = 0.1744$). No differences were seen in CD206+ cellularity over time. No direct differences were seen between Bg and WT using these markers.

CD31 staining for vascular density (Figure 2F) showed an increase in vessel formation between days 3 and 7 for both WT ($p = 0.0007$) and Bg ($p = 0.0142$) sections at the leading edge of the wounds (Figure 2G). The vessel densities of the wound bed were far lower than those at the leading edge and did not vary significantly between Bg and WT wounds at either days 3 and 7 (Figure 2H).

3 3 | Decreased collagen density in Bg wounds and increased Col1a1 gene expression

Movat's Pentachrome (Figure 3A) was used to qualitatively assess ECM constituents, such as elastin and ground substance, but no gross differences were seen. No differences were seen in average wound bed area over time (Figure 3B) when assessed by excised margins of the panniculus carnosus muscle, indicating no unintentional contracture had occurred. Cellularity in the wound bed, based on H&E staining (Figure 3C), was higher at day 7 than day 3 for both WT ($p = 0.0004$) and Bg ($p = 0.0049$) samples (Figure 3D). There were no differences in cellularity between WT and Bg wounds at either time point. Collagen was assessed by staining wound sections with Picro-Sirius Red (Figure 3E). Collagen density increased from day 3 to day 7 for both WT and Bg wounds ($p < 0.0001$ for both) (Figure 3F). The density of collagen was 10% lower at day 7 in Bg compared to WT wounds ($p = 0.0387$). In wounded samples, Col1a1 gene expression significantly increased in Bg mice at day 10 compared to days 3 and 7 ($p = 0.0141$ and $p = 0.0215$, respectively), whereas Col1a1 gene expression did not significantly change between days 3, 7, and 10 in WT mice. Col1a2

gene expression in wounded skin was significantly increased in WT mice at day 7 compared to day 3 ($p = 0.0070$), but this was not seen in Bg wounded skin (Figure 3G). Similarly, Col3a1 gene expression was relatively stable for both Bg and WT wounded skin across days 3, 7, and 10.

The degree of matrix metalloproteinases-1 (MMP-1) staining increased significantly from days 3 to 7 for both WT ($p = 0.0200$) and Bg wounds ($p = 0.0251$) (Figure 4A,B). The ratio of MMP-1 staining compared with the tissue inhibitor of metalloproteinases (TIMP-1), did not vary significantly between days 3 and 7. Positive staining of the gelatinase MMP-9 decreased from days 3 to 7 but was significant only for WT wounds ($p = 0.0049$), not for Bg ($p = 0.7686$) (Figure 4C,D). A similar trend was seen when examining the ratio of MMP-9: TIMP-1 staining, which showed only a significant decrease in WT wounds ($p = 0.0004$).

3 4 | Rate of epithelialization and barrier function are diminished in Bg mice

The epidermis was assessed with a pan-cytokeratin antibody (Figure 5A). Between days 3 and 7, WT wounds became more epithelialized ($p = 0.0015$) while Bg wounds did not ($p = 0.2127$). Bg wounds at day 7 showed significantly less epithelialization compared to WT wounds ($p = 0.0015$) (Figure 5B). Proliferation of the epithelial layers was assessed with a Ki67 antibody (Figure 5C). No differences were seen in either the fraction of Ki67+ cells to total cells or density of Ki67+ cells (Figure 5D).

To determine the effect of LYST mutation on keratinocyte barrier function, transepidermal water loss (TEWL) analysis following adhesive stripping was performed on a separate cohort of WT and Bg mice (Figure 5E). At 1-h post procedure, Bg mice had only recovered 54.0 ± 20.4% while WT mice had recovered 72.8 ± 11.3% ($p = 0.0325$). By 3 h, recovery was no longer different between groups and by 24 h barrier function returned to baseline for both groups.

3 5 | Bg fibroblasts have lower MCP-1 and IGFBP-2 in media

Media from passage one primary fibroblasts of WT and Bg mice was extracted 24 h after the first passage and applied to RayBiotech Mouse Cytokine Antibody Arrays (see Figure S2). The protein secretion assay was used to distinguish extracellular protein secretion from intracellular total protein production that predominates in vivo IHC staining. Blots of proteins of interest (Figure 6A) were measured and the relative integrated densities (Figure 6B) of monocyte chemoattractant protein-1 (MCP-1), insulin-like growth factor (IGF-1), and IGF binding protein-2 (IGFBP-2) were found to be significantly less in Bg samples ($p = 0.0083$, $p = 0.0159$, and $p = 0.0111$, respectively). Representative densities are demonstrated for factors that were not found to be significantly different (macrophage inflammatory protein-2 (MIP-2), stromal cell-derived factor 1α (SDF-1α), and IGF binding protein-3 (IGFBP-3)). There were no examples where Bg samples demonstrated a significant increase in signal. Confirmatory ELISAs were performed (Figure 6C) and Bg fibroblasts were shown to produce less MCP-1 ($p = 0.0068$) and IGFBP-2 ($p = 0.0498$) in comparison to WT fibroblasts. IGF-1 production was below the level of sensitivity for the available ELISA assay methodology. Overall, Bg fibroblasts showed a deficiency in secretion of select proteins known to be important in normal tissue healing.

3 6 | IGF-1 and IGFBP-2 gene expressions are altered in Bg fibroblasts

Lysosomes were observed with immunofluorescence of lysosome-associated membrane glycoprotein-1 (LAMP-1) and characteristic enlarged lysosomes were seen in Bg fibroblasts compared to WT fibroblasts (Figure 7A). Gene expression of LYST was not different between WT and Bg cells over a 72-h time course after the first passage (Figure 7B). MCP-1 expression was highly cytoplasmic (Figure 7C), and no differences were seen in gene expression between WT and Bg cells across time (Figure 7D). IGF-1 showed high nuclear localization with strong affinity for nucleoli (Figure 7E). Gene expression of IGF-1 (Figure 7F) was similar between WT and Bg fibroblasts for the first 48 h, but at 72 h Bg cells showed a significant increase in expression compared to WT ($p = 0.0156$). IGFBP-2 primarily localised in the nuclei of both fibroblast genotypes (Figure 7G). Gene expression of IGFBP-2 in Bg cells was downregulated compared to WT cells at 24 h ($p = 0.0083$) but normalised by 48 hours (Figure 7H). These gene expression data combined with the protein secretion data (Figure 6) suggest LYST mutation impacts gene expression and secretion of IGF-1 and IGFBP-2, but only secretion of MCP-1.

3 7 | IGF-1R co-localises with LAMP-1 on enlarged vesicles in Bg fibroblasts

IGF-1 and IGFBP-2 demonstrated colocalization in the nucleus of fibroblasts but not the cytoplasm (Figure 8A). Interestingly, IGFBP-2 was not seen in the nucleoli where IGF-1 expression was also found. IGF-1 receptor (IGF-1R) was also examined due to its role in nuclear localization of IGF-1.[32] However, IGF-1 and IGF-1R did not show colocalization (Figure 8B). IGF-1R expression appeared primarily cytoplasmic. Upon staining with LAMP-1, IGF-1R was found to colocalize on lysosomes in both cell genotypes including prominent localization on the enlarged lysosomal structures of Bg cells (Figure 8C).

3.8 | Fibroblast migration rate is unaffected by LYST mutation

To determine if migration is limited in LYST mutant cells, a scratch assay was performed on primary fibroblasts from Bg and WT mice. There were no differences in the rate of fibroblast migration over a time course of 48 h (see Figure S1).

4 | DISCUSSION

As a ubiquitously expressed, evolutionarily conserved protein, LYST is known to impact a wide range of biological processes. Indeed, the phenotype of the LYST mutant Bg mouse and patients with CHS highlights symptoms of a multi-organ system disease including disruptions of the neurologic system,[33–37] hematologic and immunologic systems,[7,15,38–40] and skin.[9] However, the role of LYST on the cutaneous wound healing response has not been investigated in either CHS patients or the Bg mouse.

In this study, we examined the effects of the Bg mutation of the LYST gene on the wound healing response in vivo utilising a splinted excisional wound model. Serial imaging and measurements of wound area closure over a 14-day period revealed that LYST mutant Bg mice had decreased closure at days 3, 10, and 14 compared to WT mice. Ultimately, Bg mice achieve wound closure, but require significantly more total days. This finding of a delayed, but ultimate complete healing response, reflects similar investigations into mouse

models of proteins critical for normal wound healing such as MCP-1, CCXR-2, MMP8, and SPARC.[41–44] We next evaluated whether the structural quality of the scar tissue in Bg mice was significantly altered after healing through mechanical testing. There were no significant differences in the max stress handled and in the stiffness of the scar tissue between Bg and WT mice 28 days post excision.

We performed histological evaluation of excised wounds at days 3 and 7 to characterise the cellular infiltration and wound remodelling process between Bg and WT mice. Bg mice have been previously described to have dysfunction of innate immune cells including macrophages.[45,46] Given the importance of phenotypically diverse pro-inflammatory/anti-inflammatory macrophages in wound healing,[47] we assessed the degree and phenotype of macrophages in excised wounds. Neutrophil (MPO+) and macrophage (F4/80+) staining revealed no direct differences in the number of macrophages present in the wound bed between Bg and WT. Staining for M1 inflammatory (iNOS+) and M2 anti-inflammatory (CD206+) markers similarly revealed no differences between Bg and WT as well. Interestingly, WT excised wounds did experience a significant decrease in macrophage (F4/80+) and neutrophil (MPO+) staining between days 3 and 7 whereas Bg saw a less robust decrease between these two time points. Additionally, Bg excised wounds experienced a significant increase in M1 inflammatory staining cells (iNOS+) between days 3 and 7 whereas WT wounds did not see such a response. These observations potentially indicate dysregulation in resolution of the normal inflammatory response to wound healing within the Bg wounds and are reflective of the delayed wound progression that is observed. Further, we did not assess for macrophage functional deficits, and it should be noted that granulocytes are known to have decreased lytic degranulation in Bg mice.[16,18,48] We evaluated neovascularization within the wound bed and the junction between normal/wounded tissue for degree of vessel formation. Quantification of CD31+ vessels revealed no differences between Bg and WT wounds at days 3 and 7. However, we acknowledge that an evaluation of later time points would increase the strength of these findings, as more time may be needed to observe differences in angiogenesis.

Extracellular matrix evaluation with Picro-Sirius Red demonstrated a decrease in collagen formation at day 7 in the Bg mice wounds. To determine if this deficiency was attributable to aberrations in collagen deposition or collagen remodelling, we analysed wound beds for MMP-1 and 9, as well as, TIMP-1. MMP-1 and MMP-9 are known to be involved in normal wound healing through extracellular matrix remodelling.[49–51] The ratios of MMP-1:TIMP-1 and MMP-9:TIMP-1 have been shown to serve as predictors of wound healing in chronic wounds, where a higher ratio of MMP-1: TIMP-1 and a faster decline in the ratio of MMP-9:TIMP-1 are predictors of robust wound healing.[52] Both Bg and WT wounds showed a similar increase in the amount of MMP-1+ staining. WT wounds had a slight elevation in MMP-1:TIMP-1 ratio between days 3 and 7 but overall neither Bg or WT had significant differences in the ratio across time. MMP-9+ expression decreased in WT wounds between days 3 and 7 but remained elevated in Bg wounds. This was also illustrated with the ratio of MMP-9:TIMP-1 staining.

We further assessed wounds for gene expression of Col1a1, Col1a2, and Col3a1 to determine if aberrant gene expression of precursors for collagen type 1 (Col1a1, Col1a2)

and collagen type 3 (Col3a1), both of which are critical components in normal skin repair following wounding, was involved in the observed delayed Bg wound collagen deposition.[53] Indeed, we found that Bg wounds had increasing Col1a1 gene expression overall in serial time points with day 10 wounds having significantly increased Col1a1 gene expression compared to days 3 and 7. In comparison, WT wounds had relatively stable Col1a1 gene expression, particularly between days 7 and 10. The increase in Col1a1 gene expression in Bg wounds, peaking at day 10, could represent a compensatory response to the decreased collagen deposition observed within the wounds of Bg mice. For both Bg and WT wounds, Col1a2 and Col3a1 gene expression was relatively stable throughout a 10-day time course indicating potentially less involvement of these collagen precursors in the observed wound healing deficit noted in Bg mice.

We assessed pan-cytokeratin to determine the degree of re-epithelialization and found that Bg mice had significantly decreased wound epithelialization at day 7. Indeed, by day 7 WT mice had achieved near 100% re-epithelization as compared to Bg mouse wounds, which were less than 50% re-epithelialized. Other models have found that delayed re-epithelization can be attributable to decreased proliferation of keratinocytes.[54,55] Therefore, we assessed the wounds with Ki67 to determine the degree of proliferating (Ki67+) cells. We found no Ki67+ differences between Bg and WT wounds at days 3 and 7 indicating that delayed epithelization was not attributable to impaired proliferation capacity of basal keratinocytes. We hypothesise that keratinocyte migration is delayed as a result of paracrine abnormalities in the wound, and not an intrinsic, structural migration defect. This is partially supported by a migration assay performed on primary fibroblasts where we observed no differences in migration rate between Bg and WT in full serum, which would mask any paracrine deficiency. However, keratinocyte migration was not directly assessed and represents an area for future investigation. It is possible that paracrine signalling from other cell types in the wound bed that wound normally stimulate keratinocyte migration is lacking. For example, elevated levels of MMP-9 have been associated with the prevention of dermal/epidermal junction reestablishment, which limits epithelial migration,[56] and elevated levels of MMP-9 were maintained in Bg wounds in contrast to WT wounds which showed a significant decline between days 3 and 7.

We considered the possibility of abnormal paracrine signalling based on the fact that LYST mutation is known to impact many cell types whose function relies on the release of granules.[7,15,33,38–40,57] This corresponds with the broader role of the endolysosomal system for protein trafficking and exocytosis. Beyond its traditional characterisation as a protein degradation organelle, lysosome function is now known to participate in diverse cellular processes including antigen presentation, plasma membrane repair, cell adhesion/migration, metabolic signalling, and protein trafficking.[58] Lysosomal trafficking to the plasma membrane is known to be impaired in LYST mutant cells,[59] potentially through the regulation of synaptotagmin-mediated Ca^{2+} sensing that facilitates lysosomal docking and exocytosis.[60] Given the increased evidence of lysosomal involvement in exocytic processes and the relevance to the complex wound healing environment,[61] we performed a cytokine screen of secreted proteins from passage one primary Bg and WT murine fibroblasts. The screen and confirmatory ELISAs highlighted a significant deficiency in MCP-1, IGFBP-2, and potentially IGF-1 secretion from Bg fibroblasts. We further investigated these findings

with immunofluorescence staining and gene expression analysis to determine if cellular localization of the proteins and gene regulation contributed to the decreased secretion. However, cellular localization and quantity was similar between Bg and WT fibroblasts for all three. Gene expression data showed no differences between WT and Bg fibroblasts across three times points (24, 48, 72 h) for MCP-1 expression. Interestingly, Bg fibroblasts had significantly increased IGF-1 gene expression data at 72 h and significantly decreased IGFBP-2 gene expression at 24 h compared to WT fibroblasts.

The in vivo findings of delayed wound healing characterised by decreased collagen deposition, epidermal barrier function, and delayed epithelization is not surprising in the context of the observed MCP-1 secretion defect from Bg fibroblasts. MCP-1$^{-/-}$ mice have a similar phenotype for abnormal wound healing that includes decreased collagen deposition, decreased re-epithelization, but with the ability to ultimately obtain healed wounds beyond 10–14 days.[41] MCP-1 is a chemokine best known for mediating the recruitment of monocytes following tissue injury.[62] Fibroblasts, monocytes, macrophages, and keratinocytes are all important sources of MCP-1 production,[63–66] and it is possible that LYST mutation impacts MCP-1 release from multiple cell types in the wound in response to injury resulting in our in vivo findings. Indeed, work aimed at attenuating MCP-1 signalling through FAK inhibition found it to reduce scar formation and collagen production in a wound healing model.[67] Similarly, MCP-1$^{-/-}$ mice do not demonstrate differences in the number of infiltrating macrophages or in the polarisation of macrophages between pro and anti-inflammatory states.

IGF-1 is a polypeptide growth factor that is involved in tissue repair and is secreted by platelets, macrophages and fibroblasts during this process.[68,69] IGF-1 increases proliferation and migration in keratinocytes and, when complexed with IGFBP-1, induces collagen contraction in fibroblasts.[70,71] By itself, IGF-1 can also stimulate wound epithelization.[72] IGF-1 expression is increased in subcutaneous and incisional wounds but is notably reduced in chronic diabetic wounds.[68,69] IGFBP-2 is a critical regulator of IGF-1 activity and transport in the pericellular space with the ability to bind IGF-1 in the ECM as a reservoir.[73] In the wound healing context, IGFBP-2 has been shown to increase migration and proliferation of dermal fibroblasts.[74] Therefore, the decreased secretion and initial decreased gene expression of IGFBP-2 observed in the Bg fibroblasts would have broader implications for IGF-1 activity.

The dynamic relationship between IGF-1, IGFBP-2, and IGF-1R, in addition to our findings that LYST mutation causes dysfunction in IGF-1/IGFBP-2 secretion and gene expression, prompted us to further examine cellular localization. The nuclear localization of IGF-1 and IGFBP-2 was similar between Bg and WT fibroblasts and supports recent work showing IGFBP-2 nuclear localization and IGF-1 nucleolus localization.[32,75,76] We observed co-localization of IGF-1R with LAMP-1 on the membrane of the enlarged lysosomes that characterise the Bg mutation, which may impact receptor trafficking. IGF-1R is internalised from the plasma membrane in endocytic vesicles and may then traverse different pathways including ubiquitination, lysosomal degradation, membrane recycling, and, nuclear localization.[77–79] While LYST mutant cells do not appear to have deficient endocytosis according to prior work,[80] the exocytic pathway may be impacted.[59] The

finding that IGF-1R heavily co-localises to enlarged Bg lysosomes raises the possibility for interruptions in IGF-1R recycling to the plasma membrane, IGF-1R trafficking for degradation, and, potentially nuclear localization.[81] This would align with recent work highlighting the role of the endolysosomal system for maintaining expression of various receptors at the plasma membrane, such as synaptic AMPA receptors.[82]

This work is not without limitations. Given the central role of the LYST protein in this study, further evaluation of the protein itself, would have provided additional insight into its involvement in our findings. However, commercially availability anti-LYST antibodies are limited, and do not have validated success across multiple experimental techniques. Additionally, our in vitro findings are limited to fibroblasts; however, we recognise that the LYST mutation affects numerous cell types in the wound bed. Indeed, our findings suggest that keratinocyte biology is particularly susceptible to disruptions in endolysosomal trafficking; and this forms the basis for future work. We initially selected primary fibroblasts as our cell type of interest due to their relevance in wound healing, and due to previous literature highlighting defective cellular processes in Bg fibroblasts.[59] We also acknowledge our fibroblasts were harvested from mouse ears instead of dorsal surface skin and there is known heterogeneity in fibroblasts.[83] Given the complexity of the wound healing response, investigating additional cell types in the context of this study would provide further insight. For example, aberrant degranulation of macrophage lytic granules and platelet dense bodies could contribute to abnormal wound healing. Conditional genetic knockout strategies of LYST will be used to evaluate these contributions in future studies. Lastly, aside from intrinsic cellular functions, LYST mutation may confer abnormal responses to extrinsic factors in the wound environment. Given the immunodeficiency observed with CHS, we highly suspect LYST mutation would confer an increased susceptibility to bacterial pathogens, which would complicate wound healing.

5 | CONCLUSIONS

The increasing incidence of problem wounds highlights the importance of identifying and characterising novel proteins that are essential to normal wound healing to provide a foundation for future therapeutic intervention. Presently, we identified for the first time that LYST is a necessary protein in normal wound healing marked its mutation leading to delayed wound closure, impaired collagen deposition, and delayed wound re-epithelization. We further demonstrated that the LYST protein is necessary for normal secretion of MCP-1, IGF-1, and IGFBP-2 from fibroblasts. While lysosomal involvement in secretory exocytosis has received recent interest, the mechanistic understanding of this process is limited. Therefore, the importance of the role of LYST in secretory exocytosis that we have described extends beyond wound healing to potentially involve a wide range of critical biological processes. Further, from a translational lens, these results identify LYST as a potential therapeutic target in disease processes characterised by dysregulated wound healing and excessive collagen production, notably hypertrophic scar and keloid formation. Future work aimed at identifying molecular intervention points for LYST regulation may provide promising therapeutic targets for modulating LYST during wound healing processes.

Supplementary Material

Refer to Web version on PubMed Central for supplementary material.

ACKNOWLEDGMENTS

K.M.B. was supported by the Tau Beta Pi 35th Centennial Fellowship. J.W.R. was supported by the American Heart Association 18POST33990231. J.C.B. was supported by NIH F32HL144120, NIH T32AI106704 and the Ohio State University President's Postdoctoral Scholar Program. A portion of this work was supported by a sponsored research agreement from LYST Therapeutics, LLC.

Funding information

American Heart Association, Grant/Award Number: 18POST33990231; LYST Therapeutics; National Institutes of Health, Grant/Award Numbers: F32HL144120, T32AI106704; Tau Beta Pi 35th Centennial Fellowship

DATA AVAILABILITY STATEMENT

The data that support the findings of this study are available from the corresponding author upon reasonable request.

REFERENCES

1. Sen CK. Human wounds and its burden: an updated compendium of estimates. Adv Wound Care 2019;8(2):39–48.
2. Perou CM, Kaplan J. Complementation analysis of Chediak-Higashi syndrome: the same gene may be responsible for the defect in all patients and species. Somat Cell Mol Genet 1993;19(5):459–468. [PubMed: 8291023]
3. Barbosa MDFS, Nguyen QA, Tchernev VT, et al. Identification of the homologous beige and Chediak-Higashi syndrome genes. Nature 1996;382(6588):262–265. [PubMed: 8717042]
4. Nagle DL, Karim MA, Woolf EA, et al. Identification and mutation analysis of the complete gene for Chediak-Higashi syndrome. Nat Genet 1996;14(3):307–311. [PubMed: 8896560]
5. Perou CM, Leslie JD, Green W, Liangtao Li H, Ward DMV, Kaplan J. The beige/Chediak-Higashi syndrome gene encodes a widely expressed cytosolic protein. J Biol Chem 1997;272(47):29790–29794. [PubMed: 9368050]
6. Jones KL, Stewart RM, Fowler M, Fukuda M, Holcombe RF. Chediak-Higashi lymphoblastoid cell lines: granule characteristics and expression of lysosome-associated membrane proteins. Clin Immunol Immunopathol 1992;65(3):219–226. [PubMed: 1333377]
7. Burkhardt JK, Wiebel FA, Hester S, Argon Y. The Giant organelles in beige and Chediak-Higashi fibroblasts are derived from late endosomes and mature lysosomes. J Exp Med 1993;178(6):1845–1856. [PubMed: 7902407]
8. Holcombe RF, Jones KL, Stewart RM. Lysosomal enzyme activities in Chediak-Higashi syndrome: evaluation of lymphoblastoid cell lines and review of the literature. Immunodeficiency 1994;5(2):131–140. [PubMed: 8032365]
9. Zhao H, Boissy YL, Abdel-Malek Z, King RA, Nordlund JJ, Boissy RE. On the analysis of the pathophysiology of Chediak-Higashi syndrome: defects expressed by cultured melanocytes. Lab Invest 1994;71(1): 25–34. [PubMed: 8041115]
10. Hammel I, Lagunoff D, Galli SJ. Regulation of secretory granule size by the precise generation and fusion of unit granules. J Cell Mol Med 2010;14(7):1904–1916. [PubMed: 20406331]
11. Kypri E, Schmauch C, Maniak M, De Lozanne A. The BEACH protein LvsB is localized on lysosomes and postlysosomes and limits their fusion with early endosomes. Traffic 2007;8(6):774–783. [PubMed: 17488289]

12. Rahman M, Haberman A, Tracy C, Ray S, Krämer H. Drosophila mauve mutants reveal a role of LYST homologs late in the maturation of phagosomes and autophagosomes. Traffic 2012;13(12):1680–1692. [PubMed: 22934826]
13. Durchfort N, Verhoef S, Vaughn MB, et al. The enlarged lysosomes in beige j cells result from decreased lysosome fission and not increased lysosome fusion. Traffic 2012;13(1):108–119. [PubMed: 21985295]
14. Cullinane AR, Schäffer AA, Huizing M. The BEACH is hot: a LYST of emerging roles for BEACH-domain containing proteins in human disease. Traffic 2013;14(7):749–766. [PubMed: 23521701]
15. Roder J, Duwe A. The beige mutation in the mouse selectively impairs natural killer cell function. Nature 1979;278(5703):451–453. [PubMed: 313007]
16. Gil-Krzewska A, Wood SM, Murakami Y, et al. Chediak-Higashi syndrome: Lysosomal trafficking regulator domains regulate exocytosis of lytic granules but not cytokine secretion by natural killer cells. J Allergy Clin Immunol 2016;137(4):1165–1177. [PubMed: 26478006]
17. Chiang SCC, Wood SM, Tesi B, et al. Differences in granule morphology yet equally impaired exocytosis among cytotoxic T cells and NK cells from Chediak-Higashi syndrome patients. Front Immunol 2017; 8(426):1–15. [PubMed: 28149297]
18. Gil-Krzewska A, Saeed MB, Oszmiana A, et al. An Actin cytoskeletal barrier inhibits lytic granule release from natural killer cells in patients with Chediak-Higashi syndrome. J Allergy Clin Immunol 2018;142(3): 914–927. [PubMed: 29241728]
19. Gene LYST lysosomal trafficking regulator [Homo sapiens (human)] Bethesda, MD: National Library of Medicine (US), National Center for biotechnology Information; 2004. https://www.ncbi.nlm.nih.gov/gene/1130
20. Galiano RD, Michaels VJ, Dobryansky M, Levine JP, Gurtner GC. Quantitative and reproducible murine model of excisional wound healing. Wound Repair Regen 2004;12(4):485–492. [PubMed: 15260814]
21. Barker JC, Barker AD, Bills J, et al. Genome editing of mouse fibroblasts by homologous recombination for sustained secretion of PDGF-B and augmentation of wound healing. Plast Reconstr Surg 2014;134(3):389–401.
22. Kreder D, Krut O, Adam-Klages S, et al. Impaired neutral sphingomyelinase activation and cutaneous barrier repair in FAN-deficient mice. EMBO J 1999;18(9):2472–2479. [PubMed: 10228161]
23. Justus CR, Leffler N, Ruiz-Echevarria M, Yang LV. In vitro cell migration and invasion assays. J Vis Exp 2014;88:51046.
24. Schindelin J, Arganda-Carreras I, Frise E, et al. Fiji: an open-source platform for biological-image analysis. Nat Methods 2012;9(7): 676–682. [PubMed: 22743772]
25. Rueden CT, Schindelin J, Hiner MC, et al. ImageJ2: ImageJ for the next generation of scientific image data. BMC Bioinform 2017; 18(1):529.
26. Hellemans J, Mortier G, De Paepe A, Speleman F, Vandesompele J. qBase relative quantification framework and software for management and automated analysis of real-time quantitative PCR data. Genome Biol 2008;8(2):R19.
27. Vandesompele J, De Preter K, Pattyn F, et al. Accurate normalization of real-time quantitative RT-PCR data by geometric averaging of multiple internal control genes. Genome Biol 2002;3(7):0034.1–0034.11.
28. Andersen CL, Jensen JL, Ørntoft TF. Normalization of real-time quantitative reverse transcription-PCR data: a model-based variance estimation approach to identify genes suited for normalization, applied to bladder and colon cancer data sets. Cancer Res 2004;64(15):5245–5250. [PubMed: 15289330]
29. Pfaffl MW, Tichopad A, Prgomet C, Neuvians TP. Determination of stable housekeeping genes, differentially regulated target genes and sample integrity: BestKeeper - Excel-based tool using pair-wise correlations. Biotechnol Lett 2004;26(6):509–515. [PubMed: 15127793]
30. Silver N, Best S, Jiang J, Thein SL. Selection of housekeeping genes for gene expression studies in human reticulocytes using real-time PCR. BMC Mol Biol 2006;7(30):1–9. [PubMed: 16412221]

31. Xie F, Xiao P, Chen D, Xu L, Zhang B. miRDeepFinder: a miRNA analysis tool for deep sequencing of plant small RNAs. Plant Mol Biol 2012;80(1):75–84.
32. Poreba E, Durzynska J. Nuclear localization and actions of the insulin-like growth factor 1 (IGF-1) system components: transcriptional regulation and DNA damage response. Mutat Res Rev Mutat Res 2020; 784:108307. 10.1016/j.mrrev.2020.108307 [PubMed: 32430099]
33. Lockman LA, Kennedy WR, White JG. The Chediak-Higashi syndrome: electrophysiological and electron microscopic observations on the peripheral neuropathy. J Pediatr 1967;70(6):942–951. [PubMed: 4290695]
34. Mathis S, Cintas P, De Saint-Basile G, Magy L, Funalot B, Vallat JM. Motor neuronopathy in Chediak-Higashi syndrome. J Neurol Sci 2014;344(1–2):203–207. [PubMed: 25043664]
35. Maaloul I, Talmoudi J, Chabchoub I, et al. Chediak-Higashi syndrome presenting in accelerated phase: a case report and literature review. Hematol Oncol Stem Cell Ther 2016;9(2):71–75. [PubMed: 26254864]
36. Introne WJ, Westbroek W, Cullinane AR, et al. Neurologic involvement in patients with atypical Chediak-Higashi disease. Neurology 2016;86(14):1320–1328. [PubMed: 26944273]
37. Lehky TJ, Groden C, Lear B, Toro C, Introne WJ. Peripheral nervous system manifestations of Chediak-Higashi disease. Muscle Nerve 2017;55(3):359–365. [PubMed: 27429304]
38. White JG. The Chediak-Higashi syndrome: a possible lysosomal disease. Blood 1966;28(2):143–156. [PubMed: 5913047]
39. Jippo-Kanemoto T, Kasugai T, Yamatodani A, et al. Supernormal histamine release and normal cytotoxic activity of beige (Chédiak-Higashi syndrome) rat mast cells with giant granules. Int Arch Allergy Immunol 1993;100(2):99–106. [PubMed: 7680258]
40. Kiyoi T, Liu S, Sahid MNA, et al. Morphological and functional analysis of beige (Chèdiak-Higashi syndrome) mouse mast cells with giant granules. Int Immunopharmacol 2019;69:202–212. [PubMed: 30738290]
41. Low QEH, Drugea IA, Duffner LA, et al. Wound healing in MIP-1$\alpha^{-/-}$ and MCP-1$^{-/-}$ mice. Am J Pathol 2001;159(2):457–463. [PubMed: 11485904]
42. Devalaraja RM, Nanney LB, Qian Q, et al. Delayed wound healing in CXCR 2 knockout mice. J Invest Dermatol 2000;115(2):234–244. [PubMed: 10951241]
43. Gutiérrez-Fernández A, Inada M, Balbín M, et al. Increased inflammation delays wound healing in mice deficient in collagenase-2 (MMP-8). FASEB J 2007;21(10):2580–2591. [PubMed: 17392479]
44. Basu A, Kligman LH, Samulewicz SJ, Howe CC. Impaired wound healing in mice deficient in a matricellular protein SPARC (osteonectin, BM-40). BMC Cell Biol 2001;2(15):1–9. [PubMed: 11178103]
45. Mahoney KH, Morse SS, Morahan PS. Macrophage functions in beige (Chédiak-Higashi syndrome) mice. Cancer Res 1980;40(11):3934–3939. [PubMed: 7471044]
46. Westphal A, Cheng W, Yu J, et al. Lysosomal trafficking regulator Lyst links membrane trafficking to toll-like receptor-mediated inflammatory responses. J Exp Med 2017;214(1):227–244. [PubMed: 27881733]
47. Krzyszczyk P, Schloss R, Palmer A, Berthiaume F. The role of macrophages in acute and chronic wound healing and interventions to promote pro-wound healing phenotypes. Front Physiol 2018;9:1–22. [PubMed: 29377031]
48. Baetz K, Isaaz S, Griffiths GM. Loss of cytotoxic T lymphocyte function in Chediak-Higashi syndrome arises from a secretory defect that prevents lytic granule exocytosis. J Immunol 1995;154(11):6122–6131. [PubMed: 7751653]
49. Rastogi A, Kim H, Twomey JD, Hsieh AH. MMP-2 mediates local degradation and remodeling of collagen by annulus fibrosus cells of the intervertebral disc. Arthritis Res Ther 2013;15(2):R57. [PubMed: 23621950]
50. Sabino F, auf dem Keller U. Matrix metalloproteinases in impaired wound healing. Met Med 2015;2:1–8.
51. Van Doren SR. Matrix metalloproteinase interactions with collagen and elastin. Matrix Biol 2015;44–46:224–231.

52. Muller M, Trocme C, Lardy B, Morel F, Halimi S, Benhamou PY. Matrix metalloproteinases and diabetic foot ulcers: the ratio of MMP-1 to TIMP-1 is a predictor of wound healing. Diabet Med 2008; 25(4):419. [PubMed: 18387077]
53. Mathew-Steiner SS, Roy S, Sen CK. Collagen in wound healing. Bioengineering 2021;8:5. [PubMed: 33466358]
54. Nishiyama T, Kii I, Kashima TG, et al. Delayed re-epithelialization in periostin-deficient mice during cutaneous wound healing. PLoS One 2011;6(4):1–14.
55. Liang X, Bhattacharya S, Bajaj G, et al. Delayed cutaneous wound healing and aberrant expression of hair follicle stem cell markers in mice selectively lacking ctip2 in epidermis. PLoS One 2012;7(2):1–15.
56. Reiss M, Han Y, Garcia E, Goldberg M, Hong Y, Garner W. Matrix Metalloproteinase-9 delays wound healing in a murine wound model. Surgery 2010;147(2):295. [PubMed: 20004432]
57. Apitz-Castro R, Cruz MR, Ledezma E, et al. The storage pool deficiency in platelets from humans with the Chédiak-Higashi syndrome: study of six patients. Br J Haematol 1985;59(3):471–483. [PubMed: 2982391]
58. Pu J, Guardia CM, Keren-Kaplan T, Bonifacino JS. Mechanisms and functions of lysosome positioning. J Cell Sci 2016;129(23):4329–4339. [PubMed: 27799357]
59. Huynh C, Roth D, Ward DM, Kaplan J, Andrews NW. Defective lysosomal exocytosis and plasma membrane repair in Chediak-Higashi/beige cells. Proc Natl Acad Sci U S A 2004;101(48):16795–16800. [PubMed: 15557559]
60. Tchernev VT, Mansfield TA, Giot L, et al. The Chediak-Higashi protein interacts with SNARE complex and signal transduction proteins. Mol Med 2002;8(1):56–64. [PubMed: 11984006]
61. Buratta S, Tancini B, Sagini K, et al. Lysosomal exocytosis, exosome release and secretory autophagy: the autophagic- and endolysosomal systems go extracellular. Int J Mol Sci 2020;21(7):2576.
62. Furie MB, Randolph GJ. Chemokines and tissue injury. Am J Pathol 1995;146(6):1287–1301. [PubMed: 7778669]
63. Matsushima K, Larsen CG, DuBois GC, Oppenheim JJ. Purification and characterization of a novel monocyte chemotactic and activating factor produced by a human myelomonocytic cell line. J Exp Med 1989;169(4):1485–1490. [PubMed: 2926331]
64. Yoshimura T, Yuhki N, Moore SK, Appella E, Lerman MI, Leonard EJ. Human monocyte chemoattractant protein-1 (MCP-1) full-length cDNA cloning, expression in mitogen-stimulated blood mononuclear leukocytes, and sequence similarity to mouse competence gene JE. FEBS Lett 1989;244(2):487–493. [PubMed: 2465924]
65. Nakamura K, Williams IR, Kupper TS. Keratinocyte-derived monocyte chemoattractant protein 1 (MCP-1): analysis in a transgenic model demonstrates MCP-1 can recruit dendritic and Langerhans cells to skin. J Invest Dermatol 1995;105(5):635–643. [PubMed: 7594634]
66. Behfar S, Hassanshahi G, Nazari A, Khorramdelazad H. A brief look at the role of monocyte chemoattractant protein-1 (CCL2) in the pathophysiology of psoriasis. Cytokine 2018;110:226–231. [PubMed: 29277337]
67. Wong VW, Rustad KC, Akaishi S, et al. Focal adhesion kinase links mechanical force to skin fibrosis via inflammatory signaling. Nat Med 2012;18(1):148–152.
68. Gartner MH, Benson JD, Caldwell MD. Insulin-like growth factors I and II expression in the healing wound. J Surg Res 1992;52(4):389–394. [PubMed: 1350650]
69. Bitar MS. Insulin-like growth factor-1 reverses diabetes-induced wound healing impairment in rats. Horm Metab Res 1997;29(8): 383–386. [PubMed: 9288575]
70. Ando Y, Jensen PJ. Epidermal growth factor and insulin-like growth factor I enhance keratinocyte migration. J Invest Dermatol 1993; 100(5):633–639. [PubMed: 8491986]
71. Lee YR, Oshita Y, Tsuboi R, Ogawa H. Combination of insulin-like growth factor (IGF)-I and IGF-binding Protein-1 promotes fibroblast-embedded collagen gel contraction. Endocrinology 1996;137(12): 5278–5283. [PubMed: 8940346]
72. Kratz G, Lake M, Gidlund M. Insulin like growth factor-1 and -2 and their role in the re-epithelialisation of wounds; interactions with insulin like growth factor binding protein type 1. Scand J Plast Reconstr Surg Hand Surg 1994;28(2):107–112. [PubMed: 7521538]

73. Yau SW, Russo VC, Clarke IJ, Dunshea FR, Werther GA, Sabin MA. IGFBP-2 inhibits adipogenesis and lipogenesis in human visceral, but not subcutaneous, adipocytes. Int J Obes (Lond) 2015;39(5):770–781. [PubMed: 25370576]
74. Brandt K, Grünler J, Brismar K, Wang J. Effects of IGFBP-1 and IGFBP-2 and their fragments on migration and IGF-induced proliferation of human dermal fibroblasts. Growth Horm IGF Res 2015;25(1):34–40. [PubMed: 25468444]
75. Azar WJ, Zivkovic S, Werther GA, Russo VC. IGFBP-2 nuclear translocation is mediated by a functional NLS sequence and is essential for its pro-tumorigenic actions in cancer cells. Oncogene 2014;33(5): 578–588. [PubMed: 23435424]
76. Durzyńska J, Wardziński A, Koczorowska M, Goździcka-Józefiak A, Barton ER. Human Eb peptide: not just a by-product of pre-pro-IGF1b processing? Horm Metab Res 2013;45(6):415–422. [PubMed: 23335048]
77. Vecchione A, Marchese A, Henry P, Rotin D, Morrione A. The Grb10/Nedd4 complex regulates ligand-induced ubiquitination and stability of the insulin-like growth factor I receptor. Mol Cell Biol 2003;23(9):3363–3372. [PubMed: 12697834]
78. Crudden C, Song D, Cismas S, et al. Below the surface: IGF-1R therapeutic targeting and its endocytic journey. Cell 2019;8(1223):1–23.
79. Girnita L, Worrall C, Takahashi SI, Seregard S, Girnita A. Something old, something new and something borrowed: emerging paradigm of insulin-like growth factor type 1 receptor (IGF-1R) signaling regulation. Cell Mol Life Sci 2014;71(13):2403–2427. [PubMed: 24276851]
80. Holland P, Torgersen ML, Sandvig K, Simonsen A. LYST affects lysosome size and quantity, but not trafficking or degradation through autophagy or endocytosis. Traffic 2014;15(12):1390–1405. [PubMed: 25216107]
81. Solomon-Zemler R, Sarfstein R, Werner H. Nuclear insulin-like growth factor-1 receptor (IGF1R) displays proliferative and regulatory activities in non-malignant cells. PLoS One 2017;12(9):e0185164. 10.1371/journal.pone.0185164 [PubMed: 28945762]
82. Parkinson GT, Hanley JG. Mechanisms of AMPA receptor endosomal sorting. Front Mol Neurosci 2018;11:440. [PubMed: 30568574]
83. Rinn JL, Bondre C, Gladstone HB, Brown PO, Chang HY. Anatomic demarcation by positional variation in fibroblast gene expression programs. PLoS Genetics 2006;2(7):1084–1096.

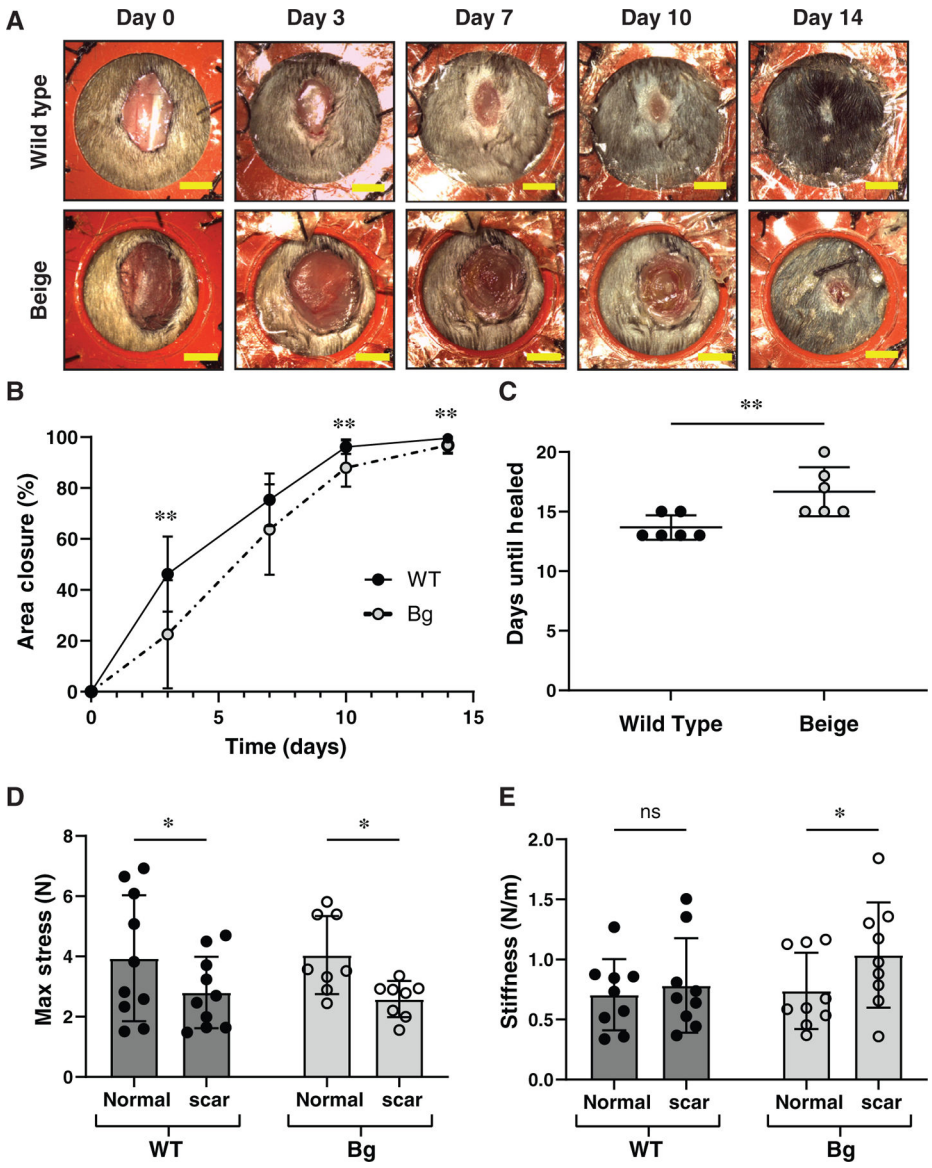

FIGURE 1.

Bg, mice have delayed wound healing. (A) Representative serial images of WT and Bg splinted, excisional wounds over the course of 2 weeks. Scale bar = 5 mm. (B) Planimetry measurements taken from serial images over time ($n = 17$ per group) show significantly less wound closure in Bg mice at 3, 10, and 14 days post procedure ($p = 0.0030$, $p = 0.0017$, and $p = 0.0082$, respectively). (C) Analysis of time needed until wounds were healed ($n = 6$ per group). Bg mice required 16.7 ± 2.1 days to heal, compared to WT mice which required 13.7 ± 1.0 days ($p = 0.0098$). (D) Mechanical testing of normal skin and scar tissue, 28 days post procedure ($n = 9$ per group). Scar tissue had a significant loss in maximum stress for both genotypes ($p = 0.0378$ for WT and $p = 0.0169$ for Bg). (E) Bg scar tissue was significantly stiffer than normal skin ($p = 0.0444$) while WT tissue demonstrated similar stiffness values between scar and normal skin. *$p \leq 0.05$, **$p \leq 0.01$ [Color figure can be viewed at wileyonlinelibrary.com]

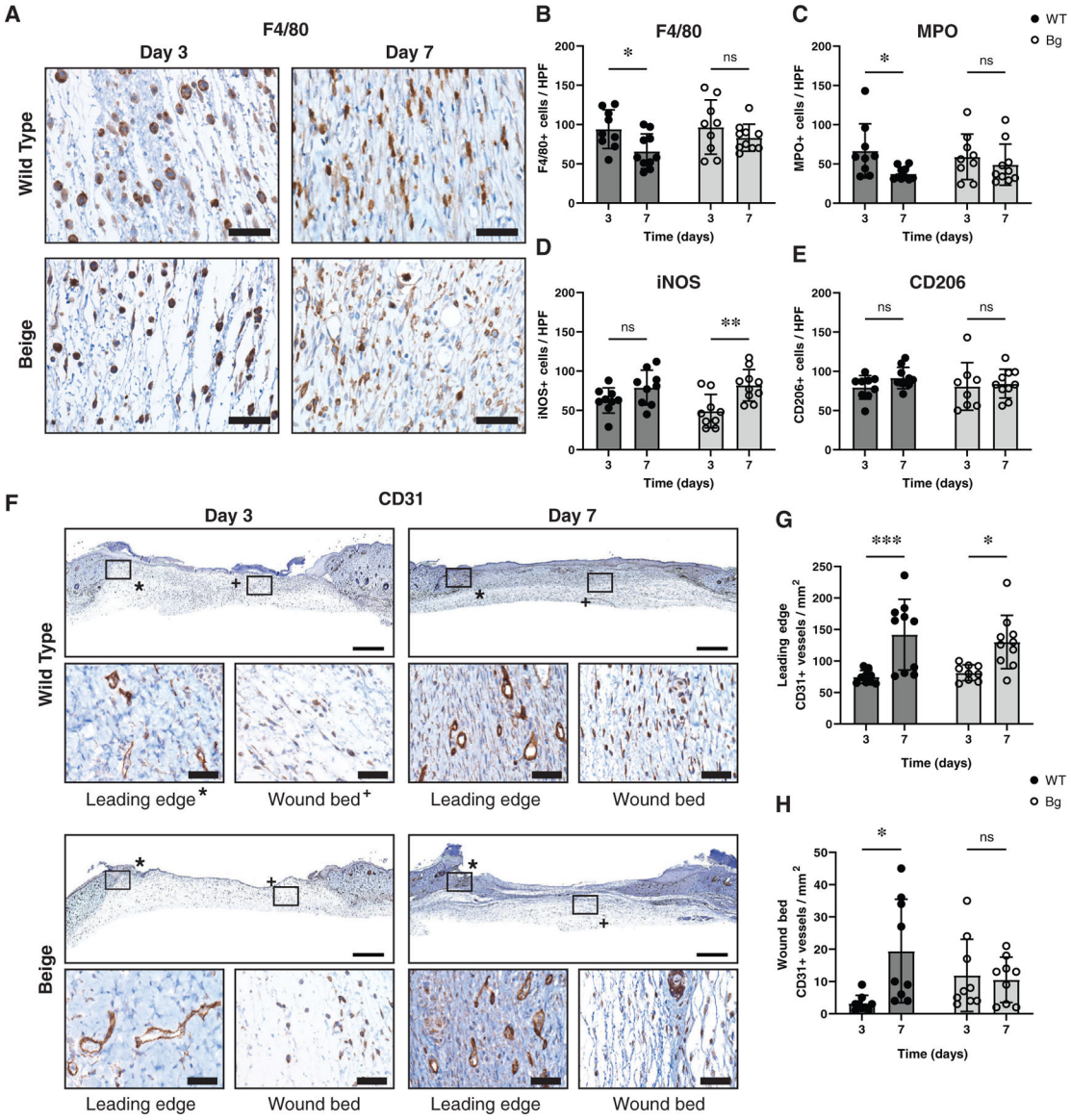

FIGURE 2.

Macrophage characterisation and wound vascularization. (A) Representative images of F4/80+ macrophage infiltration in the wounds. (B) Quantification of the number of F4/80+ cells per high powered field (HPF) show no differences between genotypes at either time point but WT did decrease between days 3 and 7 ($p = 0.0388$). (C) Similar results are seen with MPO+ neutrophils, with no differences between genotypes at either time point but WT did show a decrease between days 3 and 7 ($p = 0.0404$). (D) iNOS, an inflammatory marker, showed an increase in the number of iNOS+ cells between days 3 and 7 for Bg wounds ($p = 0.0022$) but no differences between genotypes. (E) CD206, an anti-inflammatory marker, showed no differences between genotypes or time points. (F) Whole wound sections stained to show CD31+ vessels with representative high magnification images of the leading edge of the wound (*) and the wound bed (+). (G) The number of CD31+ vessels per area in the leading edge of the wound increased between days 3 and 7 ($p = 0.0007$ for WT and $p =$

0.0142 for Bg) but no differences were seen between genotypes. (H) The number of positive vessels in the wound bed showed only an increase in vessels in WT between days 3 and 7 ($p = 0.0123$). Scale bars for high magnification images = 40 μm and low magnification images = 1 mm. *$p \leq 0.05$, **$p \leq 0.01$, ***$p \leq 0.001$ ($n = 9–10$ per group)

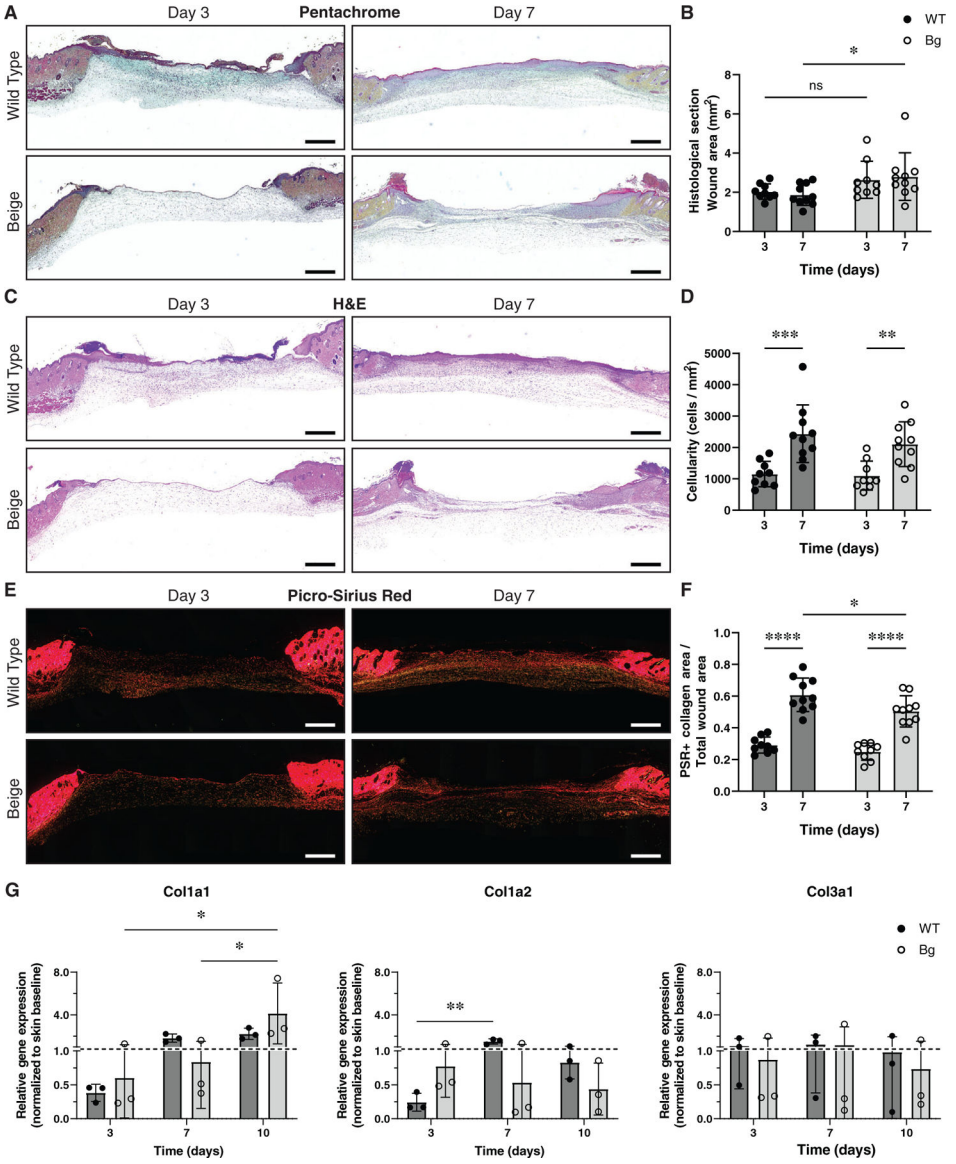

FIGURE 3.

Histological evaluation of wound cellularity and collagen deposition. (A) Sections stained with Movat's Pentachrome. No qualitative differences were observed. (B) Wound area measurements showed that average Bg wound area was larger compared to WT at day 7 (p = 0.0411). (C) Images of wound cross sections stained with H&E. (D) Wound cellularity (cells/mm^2) increased between days 3 and 7 (p = 0.0004 for WT and p = 0.0049 for Bg) but no differences were seen between genotypes. (E) Sections stained with Picro-Sirius Red and imaged with polarised light to examine collagen content of the wound area. (F) Collagen area fraction (collagen area/total area) increased between days 3 and 7 (p < 0.0001 for WT and Bg) and at day 7 Bg wounds had a significantly lower collagen area fraction compared to WT (p = 0.0387). (G) Both COL1A1 and COLA2 were under expressed in wounds at day 3 but both became upregulated in WT wounds but not in Bg. COL1A1 became upregulated in Bg wounds by day 10 but COL1a2 remained downregulated. COL3a1 fluctuated over

time but was comparable between groups. Scale bars = 1 mm. *$p \leq 0.05$, **$p \leq 0.01$, ***$p \leq 0.001$, ****$p \leq 0.0001$ (n = 9–10 per group)

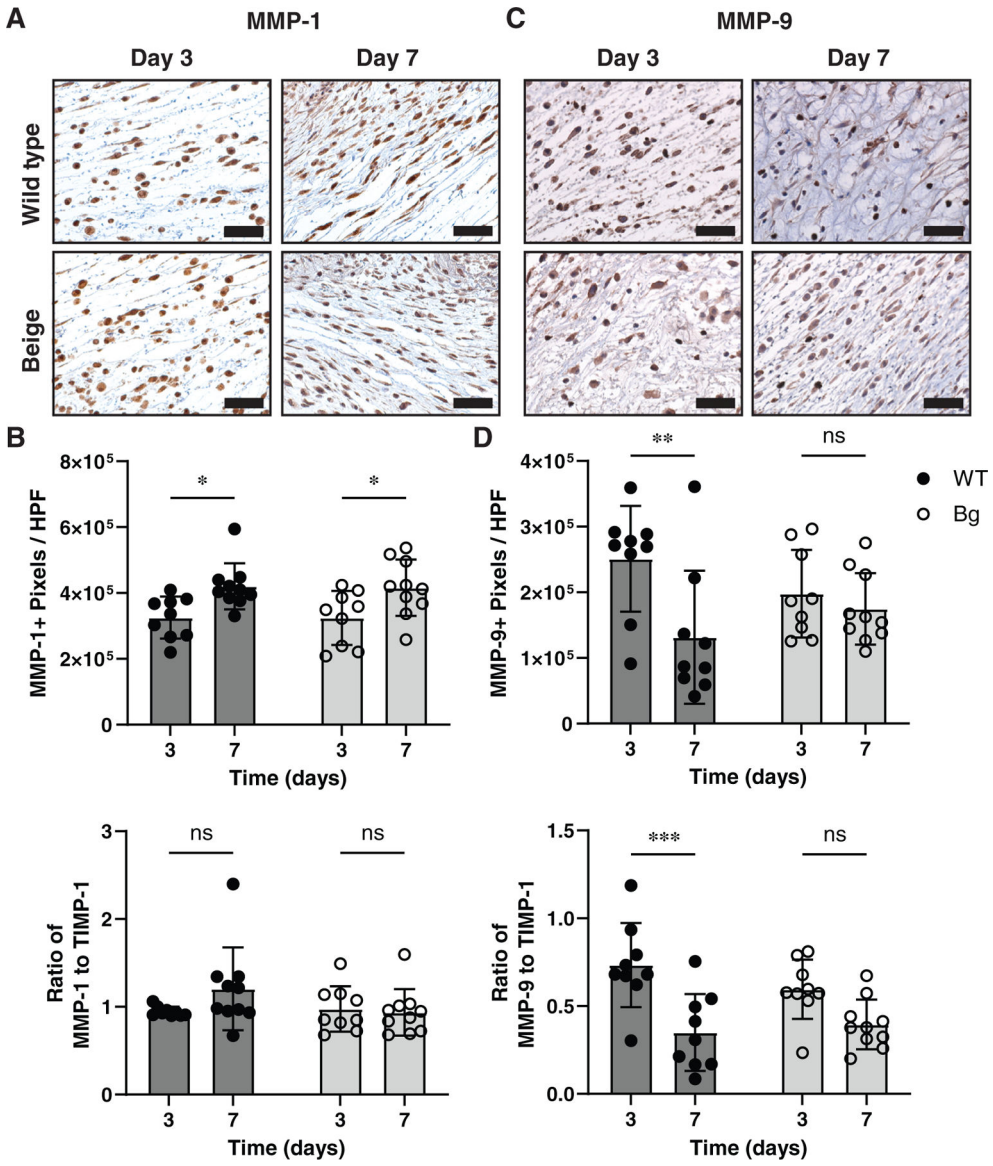

FIGURE 4.

MMP analysis. (A) Wounds sections stained for collagenase with antibody of MMP-1. (B) MMP-1+ pixels per high powered field (HPF) measurements showing an increase in positive staining with WT and Bg samples between days 3 and 7 ($p = 0.0200$ and $p = 0.0251$, respectively). (C) The ratio of MMP-1+ to TIMP-1+ staining was not different between any groups. (D) Stained sections of MMP-9, a gelatinase. (E) MMP-9+ pixels per HPF measurements show a decrease in positive staining wit WT samples between days 3 and 7 ($p = 0.0049$). (F) The same difference is seen as a ratio of MMP-9+ to TIMP-1+ staining ($p = 0.0004$). Scale bar = 40 μm. * $p \leq 0.05$, ** $p \leq 0.01$ ($n = 7$–8 per group)

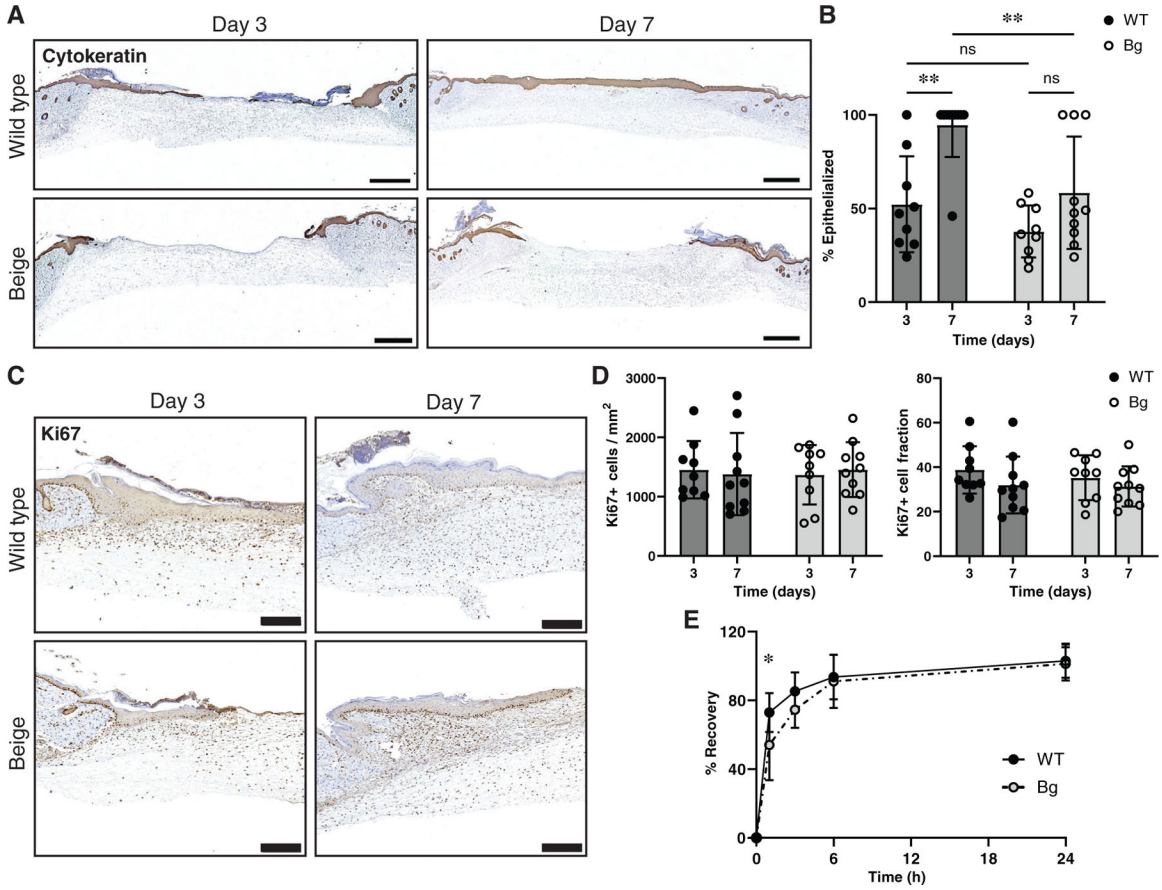

FIGURE 5.

Epithelialization, proliferation, and barrier function. (A) Tissue sections were stained with a pan-cytokeratin marker to examine the epithelialization of wounds between groups. Scale bar = 1 mm. (B) Measurements of epithelialization (cytokeratin positive cellular migration distance/full wound length) showed an increase in epithelialization in WT sections between days 3 and 7 ($p = 0.0015$) but not Bg ($p = 0.2127$). Furthermore, Bg wounds at day 7 were significantly less epithelialized compared to WT wounds at day 7 ($p = 0.0058$) ($n = 9–10$ per group). (C) Tissue stained with Ki67 were used to measure the proliferation of the epithelial layer. Scale bar = 200 μm. (D) There were no differences seen in either the number of Ki67 positive cells per area or the number of Ki67 positive cells per total cells ($n = 9–10$ per group). (E) Transepidermal water loss measurements taken showed that Bg mice had a delay in recovery of barrier function at 1-h post procedure ($p = 0.0325$) compared to WT mice. After 24 h, barrier function had been restored in both groups ($n = 7–8$ per group). *$p \leq 0.05$, **$p \leq 0.01$

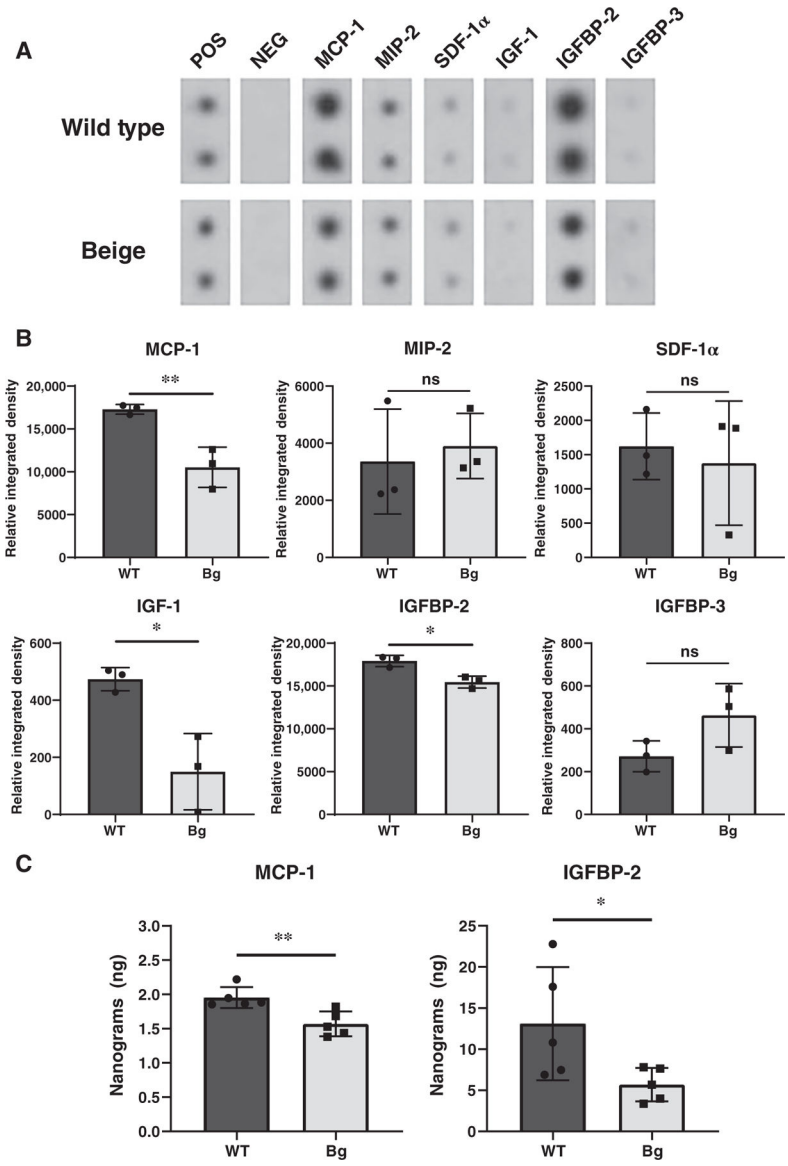

FIGURE 6.

Assessment of protein levels in conditioned media from primary fibroblast culture. (A) Representative blots of relevant cytokines, chemokines, and growth factors from RayBiotech Mouse Cytokine Antibody Arrays demonstrating WT and Bg fibroblasts' relative protein secretion in conditioned media. Fibroblasts lines were derived from 2 to 3 mice from each genotype and experiments were done with 3–5 technical replicates. (B) Quantification of the integrated densities ($n = 3$ per group). Integrated densities are relative to manufacturer controls. Relative integrated densities of MCP-1, IGF-1, and IGFBP-2 were significantly decreased in Bg samples ($p = 0.0083$, $p = 0.0159$, and $p = 0.0111$, respectively). (C) Confirmatory ELISAs of MCP-1 and IGFBP-2 ($n = 5$ per group) show decreased protein secretion from Bg fibroblasts ($p = 0.0068$ and $p = 0.0498$, respectively). *$p \leq 0.05$, **$p \leq 0.01$

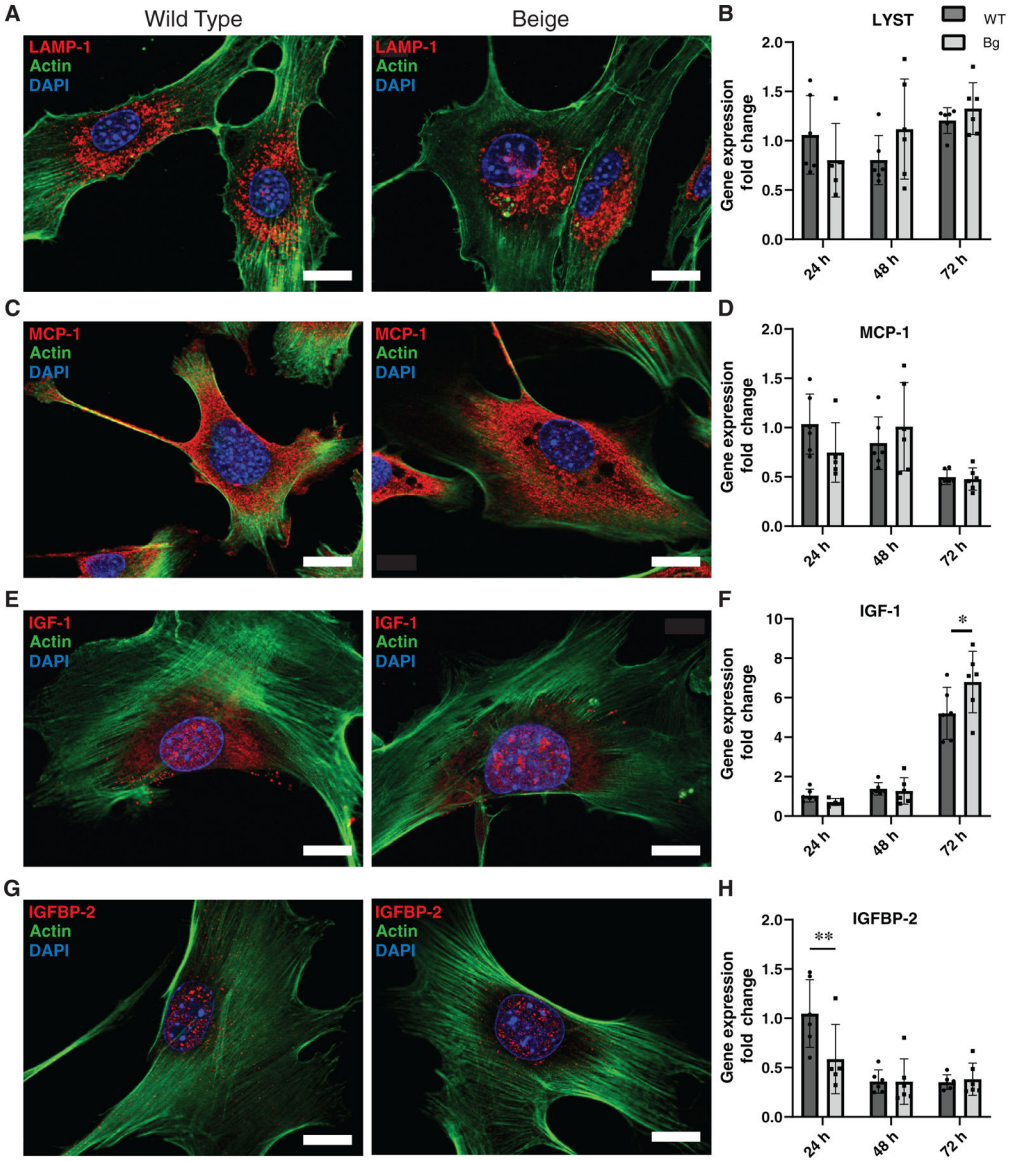

FIGURE 7.

Protein localization and gene expression in fibroblasts. (A) LAMP-1 immunofluorescent (IF) images of WT and Bg fibroblasts demonstrate enlarged lysosomes in Bg fibroblasts. (B) RT-qPCR analysis shows no change in relative gene expression of lysosomal trafficking regulator (LYST) between WT and Bg fibroblasts. (C) MCP-1 staining shows primarily cytoplasmic staining of similar degree between genotypes. (D) Gene expression of MCP-1 is comparable between genotypes at all time points. (E) Representative images of IGF-1 also show high nuclear localization with presence in nucleoli in both genotypes. (F) IGF-1 gene expression between cell types is similar at 24 and 48 h. At 72 h, Bg cells show a higher degree of gene expression ($p = 0.0156$). (G) Representative IF images of IGFBP-2 show a high degree of nuclear localization in both genotypes. (H) Relative gene expression of IGFBP-2 is decreased in Bg fibroblasts at 24 h ($p = 0.0083$) but is comparable to WT cells starting at 48 h. Fibroblasts lines were derived from 2 to 3 mice from each genotype

and experiments were done with 5–6 technical replicates. DAPI was used to visualise nuclei (blue). Actin is represented with green, and proteins of interest are red. Scale bar = 20 μm. *$p \leq 0.05$, **$p \leq 0.01$ (n = 5–6 per group)

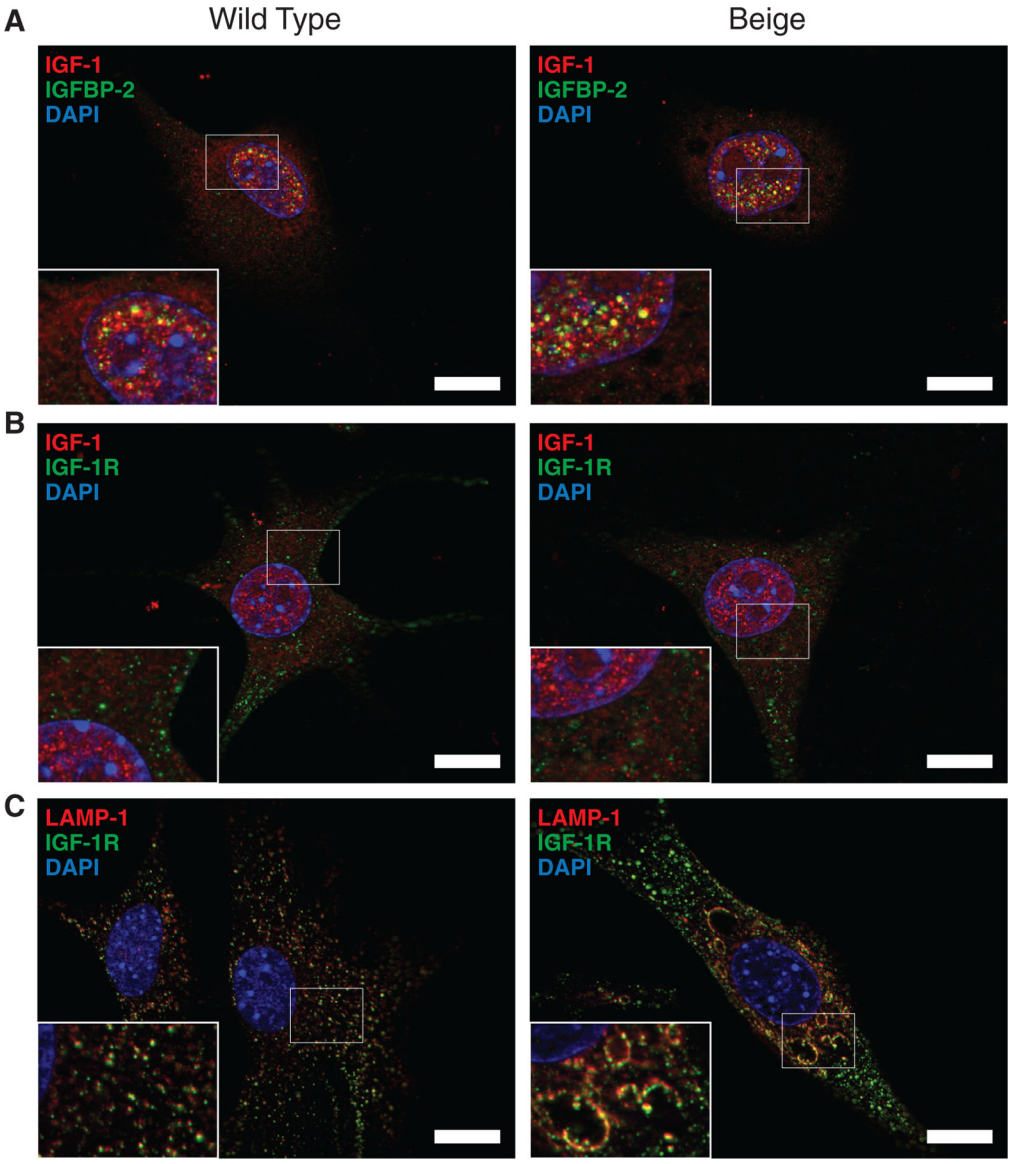

FIGURE 8.

Localization of IGF associated proteins in fibroblasts. (A) Co-stain of IGF-1 (red) and IGFBP-2 (green) shows nuclear colocalization (yellow) of the proteins based on the microscopic resolution (0.24 μm). Colocalization is not seen in the cytoplasm or in the nucleoli of the nucleus. (B) IGF-1 (red) and IGF-1 receptor (IGF-1R) (green) do not appear to colocalize. IGF-1R appears mostly cytoplasmic. (C) Lysosomes stained with LAMP-1 (red) and IGF-1R (green) show colocalization associated with the membrane of lysosomes. DAPI (blue) is used to visualise nuclei and void regions in nuclei are nucleoli. Scale bar = 20 μm